UC Riverside
UC Riverside Previously Published Works

Title
Above 400-K robust perpendicular ferromagnetic phase in a topological insulator

Permalink
https://escholarship.org/uc/item/2vr0290w

Journal
Science Advances, 3(6)

ISSN
2375-2548

Authors
Tang, Chi
Chang, Cui-Zu
Zhao, Gejian
et al.

Publication Date
2017-06-02

DOI
10.1126/sciadv.1700307

Peer reviewed

MATERIALS SCIENCE

Above 400-K robust perpendicular ferromagnetic phase in a topological insulator

Chi Tang,[1]* Cui-Zu Chang,[2,3]* Gejian Zhao,[4] Yawen Liu,[1] Zilong Jiang,[1] Chao-Xing Liu,[3] Martha R. McCartney,[4] David J. Smith,[4] Tingyong Chen,[4] Jagadeesh S. Moodera,[2,5] Jing Shi[1]†

The quantum anomalous Hall effect (QAHE) that emerges under broken time-reversal symmetry in topological insulators (TIs) exhibits many fascinating physical properties for potential applications in nanoelectronics and spintronics. However, in transition metal–doped TIs, the only experimentally demonstrated QAHE system to date, the QAHE is lost at practically relevant temperatures. This constraint is imposed by the relatively low Curie temperature (T_c) and inherent spin disorder associated with the random magnetic dopants. We demonstrate drastically enhanced T_c by exchange coupling TIs to $Tm_3Fe_5O_{12}$, a high-T_c magnetic insulator with perpendicular magnetic anisotropy. Signatures showing that the TI surface states acquire robust ferromagnetism are revealed by distinct squared anomalous Hall hysteresis loops at 400 K. Point-contact Andreev reflection spectroscopy confirms that the TI surface is spin-polarized. The greatly enhanced T_c, absence of spin disorder, and perpendicular anisotropy are all essential to the occurrence of the QAHE at high temperatures.

INTRODUCTION

The discovery of the quantum anomalous Hall effect (QAHE) in magnetically doped topological insulators (TIs) has spurred a great deal of excitement in the study of the topological state of matter (1–3). Unlike the well-known quantum Hall effect or regular AHE, the remarkable QAHE state is characterized by the quantized Hall conductance ($\pm e^2/h$) and dissipationless chiral edge current transport in the absence of any external magnetic field. Furthermore, in the QAHE state, the chiral edge charge current simultaneously carries a large and electrically tunable spin polarization due to strong spin-orbit coupling in TIs (4). These attractive properties make QAHE materials strong candidates for next-generation spintronic applications at the nanoscale.

An essential prerequisite for the QAHE to occur is an exchange interaction that breaks the time-reversal symmetry in TIs (1, 5). In a magnetically doped TI, exchange interaction originates from the long-range ferromagnetic order of magnetic moments carried by transition metal dopants, such as Cr, V, and Mn (2, 3, 6). The spontaneous magnetic order leads to an exchange gap at the Dirac point of the TI, which consequently gives rise to the QAHE. Hence, the ultimate upper temperature limit of the QAHE is dictated by the Curie temperature (T_c) of the magnetic TI. In the optimal Cr- or V-doped TI samples that exhibit QAHE, T_c can be as high as 30 K, but the QAHE only occurs at much lower temperature, that is, at or well below 2 K (2, 3, 7–9). Although the origin of this large discrepancy is an interesting topic for further investigation, it is imperative to drastically raise the T_c, and therefore greatly increase the exchange-induced gap to ultimately realize QAHE at elevated temperatures.

One possible route to higher T_c is to continue optimizing the transition metal–doping approach, similar to previous efforts in dilute magnetic semiconductor research (10). However, raising T_c requires increasing the doping level, which inevitably lowers sample quality with the presence of extensive disorder, or even destroys the nontrivial sur-

face states due to weakened spin-orbit coupling (11). An alternative route is to leverage the proximity effect to couple the TI surface states directly to a high-T_c magnetic insulator without introducing spin disorder due to randomly doped magnetic moments to either bulk or surface states. The latter approach has an obvious advantage of independent optimization of both electronic and magnetic properties (12), which is impossible in the first approach. Recent progress in this direction, including TI/EuS (13–16), $Y_3Fe_5O_{12}$(YIG)/TI (12, 17–19), and CrSb/TI (20) heterostructures, indicates its feasibility. However, although induced exchange interaction is necessary for QAHE, the in-plane magnetization in a system such as YIG/TI does not open an exchange gap in the TI surface electronic states unless reflection symmetry is broken (21). Here, we demonstrate induced ferromagnetism in TIs with perpendicular magnetic anisotropy, as manifested by sharp and squared AHE hysteresis loops, using a high-T_c (~560 K) ferrimagnetic insulator, namely, $Tm_3Fe_5O_{12}$ or TIG. In addition, the perpendicular ferromagnetic phase in TIs persists well above 400 K, which is more than one order of magnitude higher than the T_c of the optimal magnetically doped TI exhibiting QAHE. These unique features entail a much larger exchange gap in TIs without requiring any external magnetic field.

RESULTS
TIG/TI heterostructures
Similar to the YIG films in previous studies (12, 17), TIG is a rare-earth garnet with ferrimagnetism originating from the antiferromagnetically coupled iron magnetic moments via superexchange interaction. To ensure high heterostructure quality, we first prepare atomically flat TIG surfaces while engineering the needed perpendicular magnetic anisotropy. This is accomplished by epitaxial growth of TIG films on (111)-oriented substituted gadolinium gallium garnet (SGGG) substrates with pulsed laser deposition (22, 23). Because of the negative magnetostriction constant of TIG, the interface tensile strain exerted by SGGG produces perpendicular magnetic anisotropy (22). The root mean square surface roughness in 10-nm-thick TIG films can be as low as ~1.2 Å. Meanwhile, the resulting perpendicular anisotropy is sufficiently strong to drive the magnetization in the direction normal to the film plane without any external magnetic field. TIG/TI heterostructures are subsequently fabricated by growing a five–quintuple layer

[1]Department of Physics and Astronomy, University of California, Riverside, Riverside, CA 92521, USA. [2]Francis Bitter Magnet Laboratory, Massachusetts Institute of Technology, Cambridge, MA 02139, USA. [3]Department of Physics, Pennsylvania State University, University Park, PA 16802, USA. [4]Department of Physics, Arizona State University, Tempe, AZ 85287, USA. [5]Department of Physics, Massachusetts Institute of Technology, Cambridge, MA 02139, USA.
*These authors contributed equally to this work.
†Corresponding author. Email: jing.shi@ucr.edu

(QL)–thick $(Bi_xSb_{1-x})_2Te_3$ TI film atop TIG using molecular beam epitaxy (MBE) (12, 17, 24). These TI films show excellent structural quality, as confirmed by in situ reflection high-energy electron diffraction (RHEED) patterns (see fig. S1A). Ex situ high-resolution transmission electron microscopy (HRTEM) does not show any visible interfacial defects or additional phases (Fig. 1C).

The chemical potential of the TI films can be controlled by varying the Bi/Sb ratio, as demonstrated previously (25). To study the effect of carrier type on interface ferromagnetism, we deliberately choose two ratios, $x = 0.20$ and 0.30, to place the chemical potential just below and above the Dirac point, respectively. Both films behave as bulk semiconductors with the chemical potential inside the bulk gap, as indicated by the typical temperature dependence of the longitudinal sheet resistance (R_{xx}) (25), as shown in the insets of Fig. 1 (D and E). Figure 1 (D and E) shows Hall traces of these two samples measured at 400 K. Besides the clear hysteresis loops, which are further discussed below, the linear ordinary Hall background indicates opposite carrier types in these two samples, with a hole carrier density (n_{2D}) of 3.3×10^{13} cm^{-2} for $x = 0.20$ and an electron n_{2D} of 3.5×10^{13} cm^{-2} for $x = 0.30$ at $T = 400$ K. In consideration of the carrier densities below 1×10^{13} cm^{-2} at $T = 2$ K and the thermally excited additional carriers at higher temperatures, the chemical potential is located on either side of the Dirac point of the surface states but still within the bulk gap.

Anomalous Hall effect

A squared Hall hysteresis loop, which resembles the TIG magnetic hysteresis loop taken with an out-of-plane magnetic field (fig. S1B), is superimposed on the linear background. In a normal ferro- or ferrimagnetic conductor, this type of loop would be the standard anomalous

Hall signal characteristic of the ferromagnetism of the conductor (26). However, the ferrimagnet here is an insulator, and the Hall response can only come from the TI film. The hysteresis must be acquired by the bottom surface of the TI, which is in direct contact with the TIG. More representative Hall loops above room temperature are presented in Fig. 2 (low-temperature data are shown in figs. S2 and S3). The slight enhancement of the linear Hall slope at lower temperature displayed in Fig. 2 (A and C) is probably caused by a shift of the chemical potential or narrowing of the Fermi-Dirac distribution function, which changes the carrier density. After the linear ordinary Hall background is subtracted, the corresponding AHE hysteretic loops are displayed in Fig. 2 (B and D, respectively). The remarkable presence of sharp and squared loops indicates a strongly preferred perpendicular magnetization direction. Clearly, this strong perpendicular anisotropy exists throughout the entire temperature range up to 400 K (also shown in fig. S4), the highest temperature in our measurements. It is apparent from the high-temperature trend that the hysteresis extends well above 400 K, which is more than an order of magnitude higher than the record achieved in modulation-doped TI films exhibiting the QAHE (2, 3, 7–9). As the temperature decreases, the magnitude of the AHE resistance, R_{AH}, steadily increases, but the sign remains unchanged, as shown in fig. S5, which is accompanied by an increase in R_{xx}. This temperature dependence is presumably due to the reduction of bulk carriers when the temperature is lowered. It is interesting to note that the coercive fields of the two samples are different. This difference was also observed in TIG/Pt samples and attributed to the coercive field variations due to the local strain variation at the SGGG/TIG interface (22). The increased coercive field at lower temperatures results from the magnetic anisotropy increase in TIG, likely due to an enhanced magnetoelastic coefficient
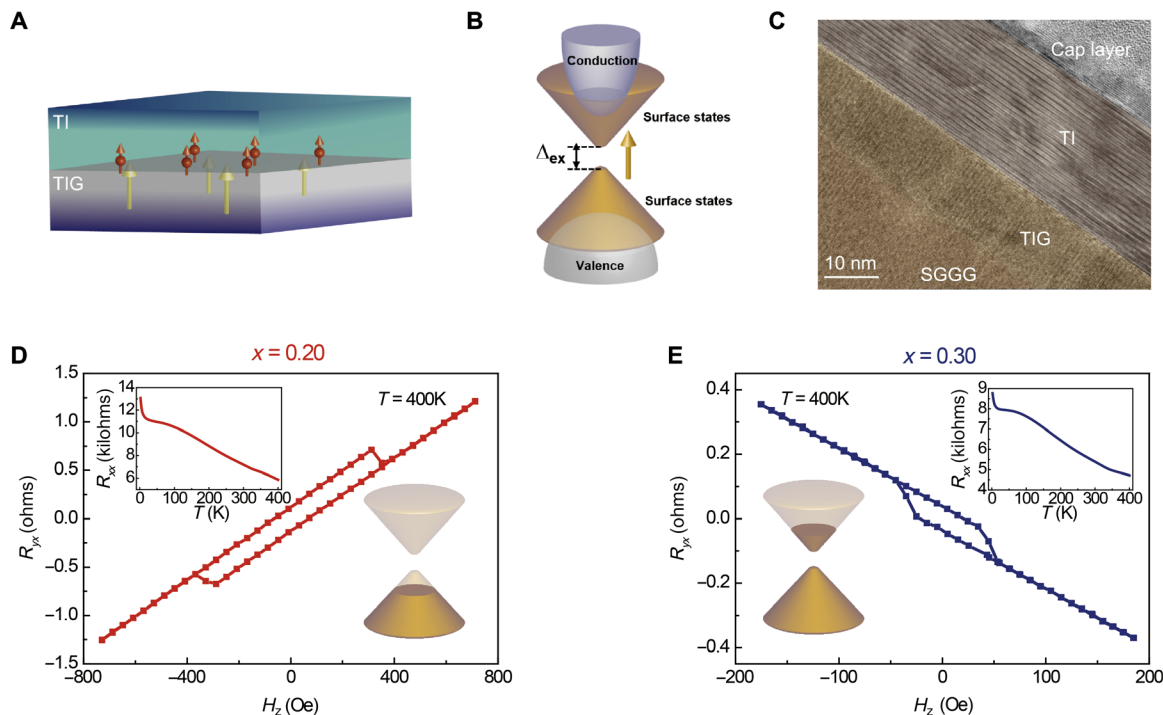

Fig. 1. Proximity-induced ferromagnetism and AHE at 400 K in TIG/TI heterostructure. (**A**) Schematic drawing of proximity coupling between TI and TIG. (**B**) Exchange gap at the charge neutral point of TI surface states induced by broken time-reversal symmetry. (**C**) HRTEM image of a TIG/TI (20 QL) bilayer structure. (**D** and **E**) Hall traces of TIG/$(Bi_xSb_{1-x})_2Te_3$ (5 QL) for $x = 0.20$ and 0.30, respectively. The upper insets show the corresponding temperature dependence of R_{xx}. The lower insets show schematic drawings of the corresponding chemical potential position.
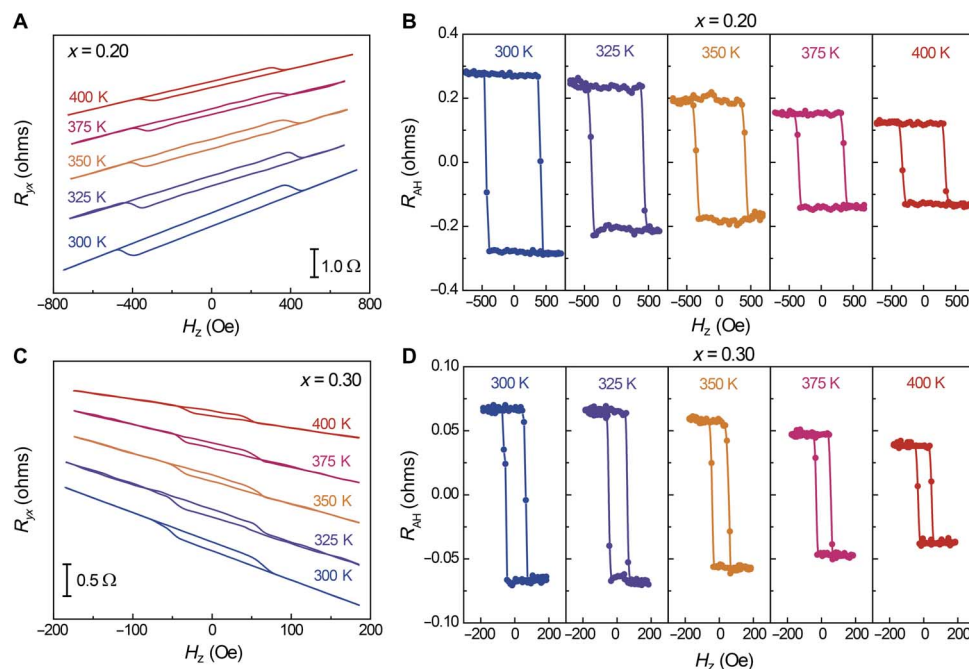
Fig. 2. Temperature dependence of AHE response up to 400 K. (**A**) Hall resistance of TIG/(Bi$_x$Sb$_{1-x}$)$_2$Te$_3$ (5 QL) for $x = 0.20$ (p-type) between 300 and 400 K. (**B**) Temperature dependence of AHE loops in (A) after subtract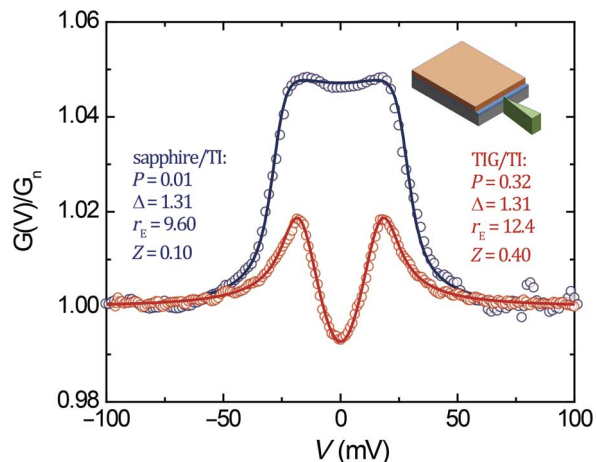ing the linear ordinary Hall background. (**C**) Hall resistance of TIG/(Bi$_x$Sb$_{1-x}$)$_2$Te$_3$ (5 QL) for $x = 0.30$ (n-type) between 300 and 400 K. (**D**) Temperature dependence of AHE loops in (C) after subtracting the linear ordinary Hall background.

Fig. 3. Representative Andreev reflection spectra for (Bi$_{0.20}$Sb$_{0.80}$)$_2$Te$_3$ (20 QL) on TIG and sapphire substrate. Fitting the normalized differential conductance to the modified BTK model yields P of 32% for TI on TIG and near-zero P for TI on sapphire. All measurements were taken at 1.5 K. The circles are raw data and solid curves are the best fits. The inset is a schematic drawing of PCAR experiments.

at low temperatures (*27*). Importantly, despite the different carrier types, the AHE loops have the same sign in these two samples. This feature immediately excludes the possibility of any Lorentz force–induced responses arising either from TIG stray fields or contributions from two types of carriers in TIs.

Spin polarization determined by Andreev reflection spectroscopy

A straightforward mechanism for the squared AHE hysteresis loops is induced ferromagnetism due to proximity coupling with TIG. Alterna-

tively, because TI has strong spin-orbit coupling, in principle, the spin Hall effect could give rise to similar AHE loops (*22*), and this scenario does not require any induced ferromagnetism in the TI. However, it is only the first mechanism that produces the exchange gap relevant to the QAHE. Magnetoresistance measurements can shed some light on the relative importance of the spin Hall effect. We have performed those measurements with both rotating and sweeping magnetic fields, and the results point toward the first mechanism (figs. S6 and S7). However, unambiguously confirming the exact mechanism with magnetotransport remains a major challenge. To directly verify the existence of induced ferromagnetism in TI surface, we use point-contact Andreev reflection spectroscopy (PCAR), a well-established probe for quantitatively measuring spin polarization in ferromagnetic materials (*28*, *29*). Because the current only flows in the TI part of the heterostructures, it exclusively detects spin polarization in the TI. To perform the measurements, we first cleaved the heterostructure sample. The superconducting tip then locates and approaches the interface from the cleaved side. Because of a limitation on tip size, the tip-sample contact is across the entire TI thickness, as shown by the inset of Fig. 3. Consequently, both the top and bottom surfaces of the TI layer contribute to the Andreev spectrum. Because of the spin-momentum locking, electrons on both TI surfaces have opposite spins in the film plane; thus, zero spin polarization is expected if both surfaces contribute equally. This is observed in the 20-QL sapphire/TI reference sample, as shown by the dark blue curve in Fig. 3. An analysis using the modified Blonder-Tinkham-Klapwijk (BTK) model (*30*) shows spin polarization (*P*) as small as 1%, which suggests slight asymmetry between two surfaces. In contrast, in TIG/(Bi$_{0.20}$Sb$_{0.80}$)$_2$Te$_3$ (20 QL), *P* is found to be more than 30% with a large interfacial factor or *Z*-factor ($Z = 0.4$), much greater than that in the reference sample. As shown in Fig. 3, the Andreev peak of the TIG/TI sample is much lower than that of the sapphire/TI, also indicating higher *P*.

DISCUSSION

In PCAR, P is often significantly reduced by having a finite interfacial scattering Z-factor. The observed P of 30% at a large Z-factor of 0.4 is therefore underestimated. Because of the difficulty in making transparent side contacts, we are unable to realize low Z-factor contacts. However, from several relatively large Z-factor contacts, we can extrapolate to an intrinsic P value of 70% at $Z = 0$ (see fig. S8), unequivocally demonstrating proximity-induced ferromagnetism in TI surface electronic states at the measurement temperature. Note that the AHE signal monotonically decreases as the temperature is increased (fig. S5), which is consistent with the decreasing trend of both induced magnetization and longitudinal resistivity. More experimental investigations are under way to directly measure the spin polarization at high temperatures.

In conclusion, we have demonstrated robust above 400-K AHE, which is dominated by proximity-induced ferromagnetism with strong perpendicular magnetic anisotropy in TI surface states of the TIG/TI heterostructures. Similar proximity-induced exchange interaction has been observed in ferromagnet/TI and antiferromagnet/TI heterostructures (12–20), but the effect in our heterostructures extends at much higher temperatures. The proximity approach offers a powerful yet flexible method to tailor both electronic and magnetic properties to realize the QAHE much above room temperatures for potential applications. The TIG/TI heterostructure also provides an ideal platform for exploring other topological magnetoelectric effects (5, 31), such as quantized Faraday and Kerr rotation (32–34) and image magnetic monopole (35).

MATERIALS AND METHODS

Thin TIG films were grown on epi-ready single-crystal SGGG (111) substrates via pulsed laser deposition. SGGG and TIG had sufficiently large lattice mismatches so that they were chosen to generate a tensile strain for inducing a large perpendicular magnetic anisotropy in TIG due to its negative magnetostriction constant. The base pressure of the deposition chamber is $\sim6 \times 10^{-7}$ torr. After going through standard cleaning, the substrates were annealed at $\sim200°C$ for over 5 hours before TIG deposition. The TIG films were then grown at a moderate temperature of $\sim500°C$ by KrF excimer laser pulses of 248 nm in wavelength with a power of 170 mJ at a repetition of 1 Hz under 2-mtorr oxygen pressure with 12 wt % ozone. Rapid thermal annealing processes were performed at 850°C for 5 min to magnetize the TIG films. Under this optimal growth condition, the as-grown TIG films exhibited strong perpendicular magnetic anisotropy, and ultraflat surfaces were characterized by vibrating sample magnetometry (fig. S1B), ferromagnetic resonance (19), and atomic force microscopy (22).

To fabricate high-quality TIG/TI heterostructures, we then transferred TIG (111) films to a custom-built ultrahigh vacuum MBE system with base pressure better than 5×10^{-10} torr for TI growth. To ensure good interface quality, we performed in situ high-temperature annealing (600°C, 60 min) before the film growth. The RHEED pattern was taken again to ensure the same excellent quality of TIG surface (fig. S1A, inset) after annealing. High-purity Bi (99.999%), Sb (99.9999%), and Te (99.9999%) were evaporated from Knudsen effusion cells. During the growth, the TIG substrate was kept at 230°C, and the growth rate was ~0.2 QL/min. The epitaxial growth was monitored by the in situ RHEED pattern. The sharp and streaky diffraction spots indicated a very flat surface and high-quality crystalline TI thin film grown on TIG (111) (fig. S1A). The film was covered with a 5-nm Te protection layer before taken out of the MBE chamber.

The HRTEM micrographs of the TIG/TI heterostructure were recorded using an image-corrected FEI Titan 80-300 operated at 300 kV, with the spherical aberration coefficient set to be $\sim+5$ μm. The specimen was cross-sectioned for observation by focused ion beam milling using an FEI dual-beam Nova 200, with initial milling at 30 kV and final surface cleaning at 5 kV.

TI films were patterned into Hall bars with width and length of 50 and 300 μm, respectively, using standard photolithography and inductively coupled plasma etching. Cr (8 nm)/Au (50 nm) was then deposited in the Hall bar contact areas for better contact. Transport measurements from 2 to 400 K were performed using a standard four-terminal dc method in a Quantum Design Physical Property Measurement System. We used a Keithley 2400 as a current source meter and a Keithley 2182A and Keithley 2000 as voltmeters. The dc source was kept constant for measurements over a temperature range but adjusted between 5 and 10 μA in different temperature ranges to avoid overheating the sample and maintain a good signal-to-noise ratio.

To perform the PCAR measurements, we deposited a gold film of ~50 nm on half of the TI sample to serve as one electrode. A few scratches were made on the sample before deposition so that the gold layer could contact both the top and bottom TI surfaces. The sample was then cleaved to create a fresh cross section and immediately mounted on a homebuilt Andreev reflection spectroscopy probe, then enclosed into a vacuum jacket, which was subsequently pumped to $\sim2 \times 10^{-7}$ torr, and then filled with a helium exchange gas of 0.1 torr. The probe was cooled down to 4.2 K in a sample tube where liquid helium was introduced through a needle valve, and 1.5 K was realized by pumping the sample tube. The point contacts were established after the temperature had been stabilized. Subsequently, the conductance (I/V) and differential conductance (dI/dV) were measured simultaneously.

SUPPLEMENTARY MATERIALS

REFERENCES AND NOTES

1. R. Yu, W. Zhang, H.-J. Zhang, S.-C. Zhang, X. Dai, Z. Fang, Quantized anomalous Hall effect in magnetic topological insulators. Science 329, 61–64 (2010).
2. C.-Z. Chang, J. Zhang, X. Feng, J. Shen, Z. Zhang, M. Guo, K. Li, Y. Ou, P. Wei, L.-L. Wang, Z.-Q. Ji, Y. Feng, S. Ji, X. Chen, J. Jia, X. Dai, Z. Fang, S.-C. Zhang, K. He, Y. Wang, L. Lu, X.-C. Ma, Q.-K. Xue, Experimental observation of the quantum anomalous Hall effect in a magnetic topological insulator. Science 340, 167–170 (2013).
3. C.-Z. Chang, W. Zhao, D. Y. Kim, H. Zhang, B. A. Assaf, D. Heiman, S.-C. Zhang, C. Liu, M. H. W. Chan, J. S. Moodera, High-precision realization of robust quantum anomalous Hall state in a hard ferromagnetic topological insulator. Nat. Mater. 14, 473–477 (2015).
4. R.-X. Zhang, H.-C. Hsu, C.-X. Liu, Electrically tunable spin polarization of chiral edge modes in a quantum anomalous Hall insulator. Phys. Rev. B 93, 235315 (2016).

5. X.-L. Qi, T. L. Hughes, S.-C. Zhang, Topological field theory of time-reversal invariant insulators. *Phys. Rev. B* **78**, 195424 (2008).

6. Y. S. Hor, P. Roushan, H. Beidenkopf, J. Seo, D. Qu, J. G. Checkelsky, L. A. Wray, D. Hsieh, Y. Xia, S.-Y. Xu, D. Qian, M. Z. Hasan, N. P. Ong, A. Yazdani, R. J. Cava, Development of ferromagnetism in the doped topological insulator $Bi_{2-x}Mn_xTe_3$. *Phys. Rev. B* **81**, 195203 (2010).

7. M. Mogi, R. Yoshimi, A. Tsukazaki, K. Yasuda, Y. Kozuka, K. S. Takahashi, M. Kawasaki, Y. Tokura, Magnetic modulation doping in topological insulators toward higher-temperature quantum anomalous Hall effect. *Appl. Phys. Lett.* **107**, 182401 (2015).

8. J. G. Checkelsky, R. Yoshimi, A. Tsukazaki, K. S. Takahashi, Y. Kozuka, J. Falson, M. Kawasaki, Y. Tokura, Trajectory of the anomalous Hall effect towards the quantized state in a ferromagnetic topological insulator. *Nat. Phys.* **10**, 731–736 (2014).

9. X. Kou, L. Pan, J. Wang, Y. Fan, E. S. Choi, W.-L. Lee, T. Nie, K. Murata, Q. Shao, S.-C. Zhang, K. L. Wang, Metal-to-insulator switching in quantum anomalous Hall states. *Nat. Commun.* **6**, 8474 (2015).

10. T. Dietl, H. Ohno, Dilute ferromagnetic semiconductors: Physics and spintronic structures. *Rev. Mod. Phys.* **86**, 187–251 (2014).

11. J. Zhang, C.-Z. Chang, P. Tang, Z. Zhang, X. Feng, K. Li, L.-l. Wang, X. Chen, C. Liu, W. Duan, K. He, Q.-K. Xue, X. Ma, Y. Wang, Topology-driven magnetic quantum phase transition in topological insulators. *Science* **339**, 1582–1586 (2013).

12. Z. Jiang, C.-Z. Chang, C. Tang, P. Wei, J. S. Moodera, J. Shi, Independent tuning of electronic properties and induced ferromagnetism in topological insulators with heterostructure approach. *Nano Lett.* **15**, 5835–5840 (2015).

13. M. Li, C.-Z. Chang, B. J. Kirby, M. E. Jamer, W. Cui, L. Wu, P. Wei, Y. Zhu, D. Heiman, J. Li, J. S. Moodera, Proximity-driven enhanced magnetic order at ferromagnetic-insulator–magnetic-topological-insulator interface. *Phys. Rev. Lett.* **115**, 087201 (2015).

14. C. Lee, F. Katmis, P. Jarillo-Herrero, J. S. Moodera, N. Gedik, Direct measurement of proximity-induced magnetism at the interface between a topological insulator and a ferromagnet. *Nat. Commun.* **7**, 12014 (2016).

15. F. Katmis, V. Lauter, F. S. Nogueira, B. A. Assaf, M. E. Jamer, P. Wei, B. Satpati, J. W. Freeland, I. Eremin, D. Heiman, P. Jarillo-Herrero, J. S. Moodera, A high-temperature ferromagnetic topological insulating phase by proximity coupling. *Nature* **533**, 513–516 (2016).

16. P. Wei, F. Katmis, B. A. Assaf, H. Steinberg, P. Jarillo-Herrero, D. Heiman, J. S. Moodera, Exchange-coupling-induced symmetry breaking in topological insulators. *Phys. Rev. Lett.* **110**, 186807 (2013).

17. Z. Jiang, C.-Z. Chang, C. Tang, J.-G. Zheng, J. S. Moodera, J. Shi, Structural and proximity-induced ferromagnetic properties of topological insulator-magnetic insulator heterostructures. *AIP Adv.* **6**, 055809 (2016).

18. M. Lang, M. Montazeri, M. C. Onbasli, X. Kou, Y. Fan, P. Upadhyaya, K. Yao, F. Liu, Y. Jiang, W. Jiang, K. L. Wong, G. Yu, J. Tang, T. Nie, L. He, R. N. Schwartz, Y. Wang, C. A. Ross, K. L. Wang, Proximity induced high-temperature magnetic order in topological insulator - ferrimagnetic insulator heterostructure. *Nano Lett.* **14**, 3459–3465 (2014).

19. W. Liu, L. He, Y. Xu, K. Murata, M. C. Onbasli, M. Lang, N. J. Maltby, S. Li, X. Wang, C. A. Ross, P. Bencok, G. van der Laan, R. Zhang, K. L. Wang, Enhancing magnetic ordering in Cr-doped Bi_2Se_3 using high-T_C ferrimagnetic insulator. *Nano Lett.* **15**, 764–769 (2015).

20. Q. L. He, X. Kou, A. J. Grutter, G. Yin, L. Pan, X. Che, Y. Liu, T. Nie, B. Zhang, S. M. Disseler, B. J. Kirby, W. Ratcliff II, Q. Shao, K. Murata, X. Zhu, G. Yu, Y. Fan, M. Montazeri, X. Han, J. A. Borchers, K. L. Wang, Tailoring exchange couplings in magnetic topological-insulator/antiferromagnet heterostructures. *Nat. Mater.* **16**, 94–100 (2017).

21. X. Liu, H.-C. Hsu, C.-X. Liu, In-plane magnetization-induced quantum anomalous Hall effect. *Phys. Rev. Lett.* **111**, 086802 (2013).

22. C. Tang, P. Sellappan, Y. Liu, Y. Xu, J. E. Garay, J. Shi, Anomalous Hall hysteresis in $Tm_3Fe_5O_{12}$/Pt with strain-induced perpendicular magnetic anisotropy. *Phys. Rev. B* **94**, 140403(R) (2016).

23. C. O. Avci, A. Quindeau, C.-F. Pai, M. Mann, L. Caretta, A. S. Tang, M. C. Onbasli, C. A. Ross, G. S. D. Beach, Current-induced switching in a magnetic insulator. *Nat. Mater.* **16**, 309–314 (2017).

24. Z. Jiang, C.-Z. Chang, M. R. Masir, C. Tang, Y. Xu, J. S. Moodera, A. H. MacDonald, J. Shi, Enhanced spin Seebeck effect signal due to spin-momentum locked topological surface states. *Nat. Commun.* **7**, 11458 (2016).

25. J. Zhang, C.-Z. Chang, Z. Zhang, J. Wen, X. Feng, K. Li, M. Liu, K. He, L. Wang, X. Chen, Q.-K. Xue, X. Ma, Y. Wang, Band structure engineering in $(Bi_{1-x}Sb_x)_2Te_3$ ternary topological insulators. *Nat. Commun.* **2**, 574 (2011).

26. N. Nagaosa, J. Sinova, S. Onoda, A. H. MacDonald, N. P. Ong, Anomalous Hall effect. *Rev. Mod. Phys.* **82**, 1539 (2010).

27. S. Iida, Magnetostriction constants of rare earth iron garnets. *J. Phys. Soc. Jpn.* **22**, 1201–1209 (1967).

28. R. J. Soulen Jr., J. M. Byers, M. S. Osofsky, B. Nadgorny, T. Ambrose, S. F. Cheng, P. R. Broussard, C. T. Tanaka, J. Nowak, J. S. Moodera, A. Barry, J. M. D. Coey, Measuring the spin polarization of a metal with a superconducting point contact. *Science* **282**, 85–88 (1998).

29. L. Wang, K. Umemoto, R. M. Wentzcovitch, T. Y. Chen, C. L. Chien, J. G. Checkelsky, J. C. Eckert, E. D. Dahlberg, C. Leighton, $Co_{1-x}Fe_xS_2$: A tunable source of highly spin-polarized electrons. *Phys. Rev. Lett.* **94**, 056602 (2005).

30. T. Y. Chen, S. X. Huang, C. L. Chien, Pronounced effects of additional resistance in Andreev reflection spectroscopy. *Phys. Rev. B* **81**, 214444 (2010).

31. A. M. Essin, J. E. Moore, D. Vanderbilt, Magnetoelectric polarizability and axion electrodynamics in crystalline insulators. *Phys. Rev. Lett.* **102**, 146805 (2009).

32. L. Wu, M. Salehi, N. Koirala, J. Moon, S. Oh, N. P. Armitage, Quantized Faraday and Kerr rotation and axion electrodynamics of a 3D topological insulator. *Science* **354**, 1124–1127 (2016).

33. W.-K. Tse, A. H. MacDonald, Giant magneto-optical Kerr effect and universal Faraday effect in thin-film topological insulators. *Phys. Rev. Lett.* **105**, 057401 (2010).

34. J. Maciejko, X.-L. Qi, H. D. Drew, S.-C. Zhang, Topological quantization in units of the fine structure constant. *Phys. Rev. Lett.* **105**, 166803 (2010).

35. X.-L. Qi, R. Li, J. Zang, S.-C. Zhang, Inducing a magnetic monopole with topological surface states. *Science* **323**, 1184–1187 (2009).